

# Higher Josephson harmonics in a tunable double-junction transmon qubit

Ksenia Shagalov,<sup>1, 2,\*</sup> David Feldstein-Bofill,<sup>1, 2</sup> Leo Uhre Jakobsen,<sup>1, 2</sup> Zhenhai Sun,<sup>1, 2</sup> Casper Wied,<sup>1, 2</sup> Amalie T. J. Paulsen,<sup>1, 2</sup> Johann Bock Severin,<sup>1, 2</sup> Malthe A. Marciniak,<sup>1, 2</sup> Clinton A. Potts,<sup>1, 2</sup> Anders Kringhøj,<sup>1, 2</sup> Jacob Hastrup,<sup>1, 2</sup> Karsten Flensberg,<sup>1</sup> Svend Krøjer,<sup>1, 2</sup> and Morten Kjaergaard<sup>1, 2, †</sup>

<sup>1</sup>Center for Quantum Devices, Niels Bohr Institute, University of Copenhagen, Denmark  
<sup>2</sup>NNF Quantum Computing Programme, Niels Bohr Institute, University of Copenhagen, Denmark

(Dated: December 12, 2025)

Tunable Josephson harmonics open new avenues for qubit design. We demonstrate a superconducting circuit element consisting of a tunnel junction in series with a SQUID loop, yielding a Josephson potential whose harmonic content is strongly tunable by magnetic flux. Through spectroscopy of the first four qubit transitions, together with an effective single-mode model renormalized by the internal mode, we resolve a second harmonic with an amplitude up to  $\sim 10\%$  of the fundamental. We identify a flux sweet spot where the dispersive shift vanishes, achieved by balancing the dispersive couplings to the internal and qubit modes. This highly tunable element provides a route toward protected qubits and customizable nonlinear microwave devices.

Superconductor–insulator–superconductor (SIS) Josephson junctions (JJs) form the nonlinear element in most superconducting circuits [1]. The corresponding Josephson potential is conventionally modeled by a single harmonic,  $U(\phi) = -E_J \cos \phi$ , with  $E_J$  the Josephson energy [2], which underpins key circuit properties, including anharmonicity and charge-noise sensitivity. However, recent experiments have shown that SIS junctions can exhibit higher harmonics, i.e. terms proportional to  $\cos(k\phi)$  with  $k > 1$ , arising from pinholes in the junction or from inductive contributions of the leads [3–6].

Generalizing these observations, the potential of a superconducting Josephson element can be described through a Fourier series,

$$U(\phi) = \sum_{k=1}^{\infty} U_k \cos(k\phi), \quad (1)$$

where  $U_k$  are the harmonic coefficients with the  $k$ 'th term corresponding to transmission of  $k$  pairs of Cooper-pairs across the junction [7]. Controlling the ratio between the first and higher Josephson harmonics thus enables modifications of the potential energy landscape of a superconducting circuit. Importantly, higher harmonic engineering has enabled the design of protected qubits with suppressed sensitivity to charge or flux noise [8–11] and superconducting diodes [12–14].

One approach toward generating higher Josephson harmonics uses superconductor–normal-metal–superconductor (SNS) junctions [15] and hybrid superconductor–semiconductor weak links [16]. In SNS elements, multiple Andreev reflections enable multi-Cooper-pair tunneling, producing a strongly non-sinusoidal potential [17] with a substantially higher-harmonic content [8, 18, 19]. Such junctions have been

used to demonstrate gate-tunable qubits [20, 21],  $\Phi_0$ -junctions [22], and diode-like behavior [13, 14]. However, hybrid platforms often suffer from frequency instability and reduced coherence, potentially due to losses in the semiconducting region [23].

Another approach relies on placing two SIS junctions in series, a configuration previously employed for flux-noise suppression in tunable transmons [24–26], dephasing-protected readout [27], and scalable JJ fabrication schemes [28]. The effective energy-phase relation in this configuration under suitable approximations resembles that of an SNS junction with a single transmission channel [29], yielding a non-sinusoidal potential with its shape set by the asymmetry of the two junction energies. Experiments conducted on InAs/Al hybrid heterostructures have shown that adjusting the junction asymmetry through gate tuning can modify the energy-phase relation from a sinusoidal form to one that closely resembles the SNS junction [30].

In this manuscript, we demonstrate a device capable of *in situ* control of the energy-phase relation using only SIS junctions. The device is a tunable double-junction transmon composed of a superconducting quantum interference device (SQUID) [31, 32] in series with a single JJ and shunted by a large capacitor, allowing the junction asymmetry parameter  $\lambda$  to be tuned via the external magnetic flux  $\Phi_e$ . Spectroscopy of higher-order qubit transitions shows an enhanced higher-harmonic contribution compared to previously reported values in SIS junctions [3–6]. A model including an auxiliary (internal) mode, associated with the superconducting island between the JJ and SQUID, captures the data and accounts for a renormalization of the qubit frequency. We also find that this internal mode couples dispersively to the readout resonator, leading to a flux point where the total ground-state dispersive shift cancels.

Figure 1a shows a circuit diagram of the tunable double-junction transmon, with the scanning electron microscope (SEM) images of the corresponding fabricated device shown in Figs. 1b, c (fabrication details can be

\* ksenia.shagalov@nbi.ku.dk

† mkjaergaard@nbi.ku.dk

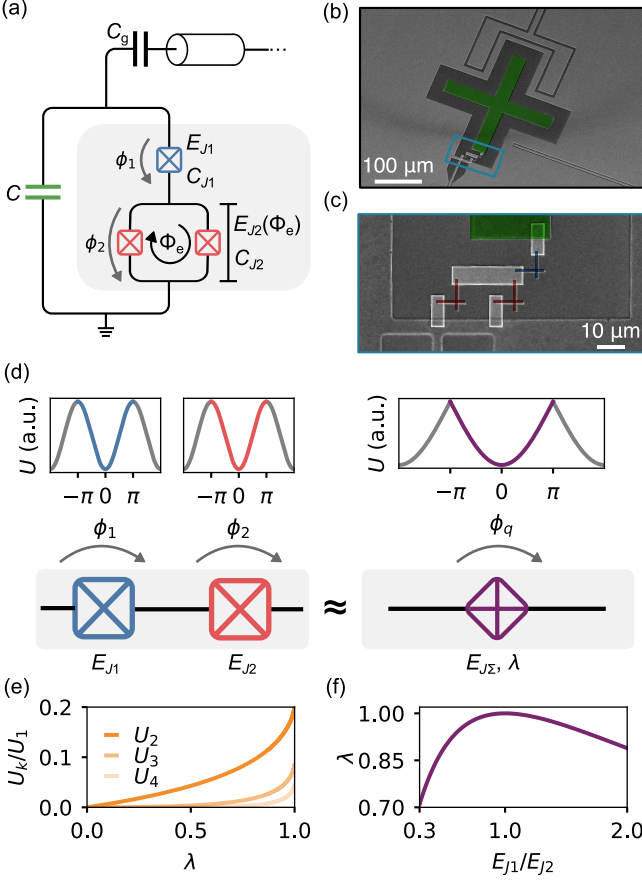


FIG. 1. Qubit circuit and device design. (a) Circuit schematic of the tunable double-junction transmon with a single JJ (blue) and a SQUID loop (red) in series, shunted by a large capacitor (green). (b) SEM of the tunable double-junction transmon showing the large island which forms the capacitor (green). A quarter-wave resonator is capacitively coupled to the qubit for readout. A flux line threads magnetic flux through the SQUID loop, and the drive line facilitates the XY control. (c) SEM image of the single JJ (blue) and the SQUID loop (red) in series. (d) The potentials  $U$  plotted for each SIS junction (blue, red), which in series effectively correspond to the potential from Eq. 2, shown for  $\lambda = 1$  (purple). (e) Harmonic content of the potential from Eq. 2 as a function of  $\lambda$ . (f)  $\lambda$  as a function of the ratio between the Josephson energies of the two junctions.

found in the Supplementary material [33]). We denote by  $\phi_1$  and  $\phi_2$  the superconducting phases across the single junction and the SQUID, respectively. To understand the origin of the appreciable higher harmonics in an SIS–SIS device, we consider a “reduced” model in which the charging energy of the middle island is initially omitted. In this limit, the two junctions behave as a single effective element with a potential of the form [29]

$$U_{\text{red.}}(\phi_q) = -E_{J\Sigma} \sqrt{1 - \lambda \sin^2(\phi_q/2)}, \quad (2)$$

where  $\phi_q = \phi_1 + \phi_2$  is the phase of the qubit mode,

$E_{J\Sigma} = E_{J1} + E_{J2}$ , and

$$\lambda = 4E_{J1}E_{J2}/(E_{J1} + E_{J2})^2 \quad (3)$$

is the junction asymmetry parameter. The resulting potential landscape in this reduced model is shown in Fig. 1d. The emergence of higher harmonics becomes explicit in the symmetric case  $E_{J1} = E_{J2}$ , where  $\lambda = 1$  and Eq. (2) expands to

$$U_{\text{red.}}(\phi_q) = E_{J\Sigma} \sum_k \left[ (-1)^{k+1} \frac{4}{\pi - 4\pi k^2} \right] \cos(k\phi_q), \quad (4)$$

identifying the coefficients in brackets with  $U_k$  from Eq. (1). Figure 1e shows that the second harmonic can reach  $|U_2/U_1| \approx 0.2$  at  $\lambda = 1$  [34], substantially larger than previously reported values for single SIS junctions [3–6]. Conversely, for  $\lambda \ll 1$ , the familiar sinusoidal form is recovered:  $U_{\text{red.}}(\phi_q) \propto \cos \phi_q$ . Figure 1f shows how  $\lambda$  varies with  $E_{J1}/E_{J2}$ , reflecting its role as the junction asymmetry parameter, analogous to the effective transmission  $\tau$  of a single Andreev mode in the SNS potential  $U_{\text{SNS}}(\phi) = -\Delta \sqrt{1 - \tau \sin^2(\phi/2)}$  where  $\Delta$  is the superconducting gap [35].

In the tunable double-junction transmon, threading the external flux through the SQUID loop makes the junction asymmetry parameter flux dependent,  $\lambda \rightarrow \lambda(\Phi_e)$ , and thereby allows *in situ* control of the effective potential and its harmonic content. As Fig. 1f shows,  $\lambda$  varies slowly near  $E_{J1}/E_{J2} \approx 1$ , so precise flux biasing to the symmetric point is not required for higher harmonics to be appreciable. In practice, whenever  $E_{J2}(\Phi_e)$  lies within roughly a factor of two of  $E_{J1}$ , the asymmetry parameter remains above  $\lambda \approx 0.9$ , corresponding to a second-harmonic ratio of  $|U_2/U_1| \approx 0.12$ .

In Fig. 2a we show the  $f_{01}$ ,  $f_{02}$ ,  $f_{03}$ , and  $f_{04}$  transitions of the tunable double-junction transmon as a function of flux threading the SQUID loop, obtained using two-tone spectroscopy in the second cooldown of the device. To fit the spectra, we use a two-mode Hamiltonian that includes both phase degrees of freedom across each junction,

$$H_{\text{full}} = 4E_{C1}n_1^2 + 4E_{C2}n_2^2 + g_{12}n_1n_2 + U_{\text{red.}}(\phi_1, \phi_2), \quad (5)$$

with

$$U_{\text{red.}}(\phi_1, \phi_2) = -E_{J1} \cos(\phi_1) - E_{J2} \cos(\phi_2), \quad (6)$$

where  $E_{C1}$ ,  $E_{C2}$ ,  $g_{12}$  and a detailed circuit analysis can be found in the Supplementary Material [33]. We perform a simultaneous fit to all measured  $f_{01}$  and  $f_{02}/2$  values, extracting the island capacitance as well as the capacitances and Josephson energies of the individual junctions. The resulting fit is shown as the solid line in Fig. 2a. Using these fitted parameters, the model also predicts  $f_{03}$  and  $f_{04}$  with excellent agreement (dotted gray lines). Further details of the fitting procedure are provided in Supplementary Material [33] (Figs. 5, 6). Overall, the

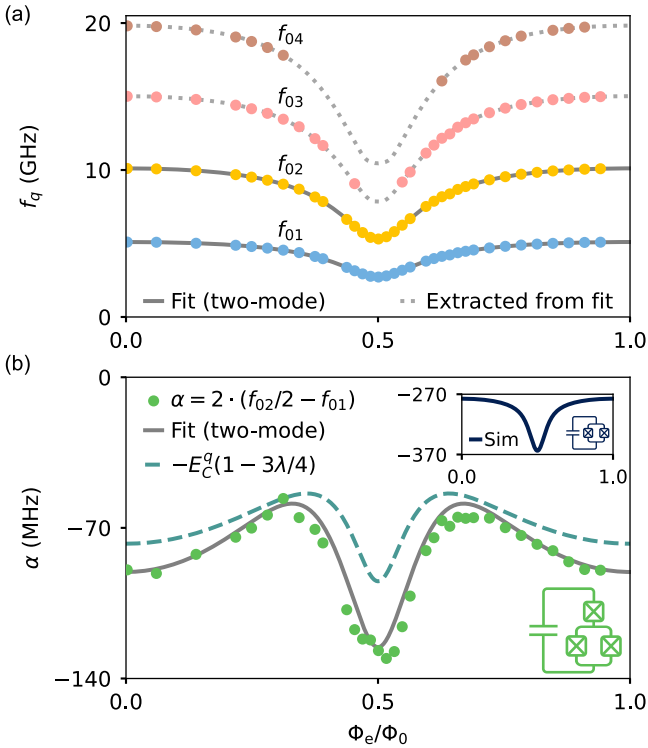


FIG. 2. Flux-dependent two-tone spectroscopy of the tunable double-junction transmon (second cooldown) and fit using the two-mode model from Eq. 5. (a) Two-tone spectroscopy of the  $f_{01}$  (light blue),  $2 \cdot f_{02}/2$  (yellow),  $3 \cdot f_{03}/3$  (pink) and  $4 \cdot f_{04}/4$  (brown) transitions as a function of  $\Phi_e$ . The  $f_{01}$  and  $f_{02}$  transitions are fitted to the two-mode model of Eq. 5 (solid gray), and the resulting parameters are used to predict  $f_{03}$  and  $f_{04}$  (dotted gray). (b) Extracted anharmonicity (green) obtained from the  $f_{01}$  and  $f_{02}/2$  transitions together with the corresponding fit (solid gray). The analytical expression from Eq. 8, based on the potential in Eq. 2, is shown for comparison (dashed teal). Inset: simulated anharmonicity versus flux for a tunable transmon with comparable device parameters.

two-mode model captures both the qualitative structure and the quantitative values of the observed spectra.

In Fig. 2b, we extract the flux-dependent anharmonicity via,  $\alpha = 2(f_{02}/2 - f_{01})$ , shown as green circles. The solid line is the anharmonicity obtained from the fit in Fig. 2a, again demonstrating good agreement between the two-mode model and the measured spectra. The anharmonicity of the tunable double-junction transmon exhibits a pronounced *non-monotonic* dependence on flux between  $\Phi_e = 0$  and  $\Phi_e = \Phi_0/2$ . That is in sharp contrast to a conventional flux-tunable transmon for which the anharmonicity monotonically depends on flux [36] (see inset of Fig. 2b for a simulation using the same  $E_C$  and  $E_J$ s that would provide the same frequency tunability range as for the tunable-double junction transmon). Notably, at  $\Phi_e = 0$  the tunable double-junction transmon reaches  $h\alpha \approx -E_C/3$  (Fig. 2b), deviating significantly from the pure transmon value of  $h\alpha \approx -E_C$  [36].

The qualitative difference between the anharmonicity of the tunable double-junction transmon and that of a traditional flux-tunable transmon can be understood from the reduced model of Eq. (2). Using the reduced potential, the Hamiltonian of the qubit mode is

$$H_{\text{red.}} = 4E_C^q n_q^2 + U_{\boxtimes\boxtimes}^{\text{red.}}(\phi_q), \quad (7)$$

where  $E_C^q = e^2/[2(C+C_{J1}C_{J2}/(C_{J1}+C_{J2}))]$  is the charging energy of the qubit mode. Applying the transmon approximation ( $E_{J\Sigma}/E_C^q \gg 1$ ) and expanding  $U_{\boxtimes\boxtimes}^{\text{red.}}(\phi_q)$  to fourth order yields  $h\alpha \approx \sqrt{8E_C^q E_J^{\text{eff}}} - h\alpha$ , with  $E_J^{\text{eff}} = E_{J1}E_{J2}/(E_{J1} + E_{J2})$ , and an anharmonicity

$$h\alpha \approx -E_C^q \left(1 - \frac{3}{4}\lambda\right), \quad (8)$$

result previously demonstrated from studying anharmonicity in gatemons [37]. Figure 2b shows Eq. (8) (teal dashed line) evaluated using the parameters extracted from the two-mode fit. The remaining discrepancy between Eq. (8) and the measured anharmonicity arises from the limitations of the transmon approximation and from the internal mode, which renormalizes the qubit spectrum.

We now investigate the presence of higher harmonics in the tunable double-junction transmon. In the two-mode model (Eq. (5)), each junction is described by a sinusoidal potential; thus, the higher harmonics in the reduced model (Eq. (7)) emerge from the single-mode picture, analogous to the effective linear inductance of junction-array superinductors [38, 39]. However, the reduced model does not reproduce the measured spectra with sufficient accuracy and therefore cannot be used to reliably extract harmonic content (see Supplementary Material [33], Fig. 6). To assess higher harmonics of the qubit mode  $\phi_q$ , we therefore derive an approximate single-mode model that incorporates the leading-order effect of the internal mode.

In the situation where the excitations in the internal mode are higher in frequency than the first few qubit excitations, we can apply a Born-Oppenheimer (BO) approximation to describe the low-energy spectrum of the qubit [40, 41]. In this approximation, the ground-state energy of the internal mode depends parametrically on  $\phi_q$  and therefore acts as an effective potential for the qubit mode. Within an analytical BO approximation framework, we can utilize that the internal mode is transmon-like, i.e.  $E_C^{\text{int}}/E_{J\Sigma} \ll 1$ , resulting in a BO correction due to the internal mode, up to first order in  $E_C^{\text{int}}/E_{J\Sigma}$ , given by [34],

$$U_{\boxtimes\boxtimes}^{\text{BO}}(\phi_q) = E_{J\Sigma} \sqrt{\frac{2E_C^{\text{int}}}{E_{J\Sigma}}} \sqrt{1 - \lambda \sin^2(\phi_q/2)}, \quad (9)$$

where  $E_C^{\text{int}} = e^2/[2(C_{J1} + C_{J2})]$  is the charging energy of the internal mode and  $E_C^{\text{int}}/E_{J\Sigma} \sim 1/300$  for our experimental parameters. Thus, our BO one-dimensional

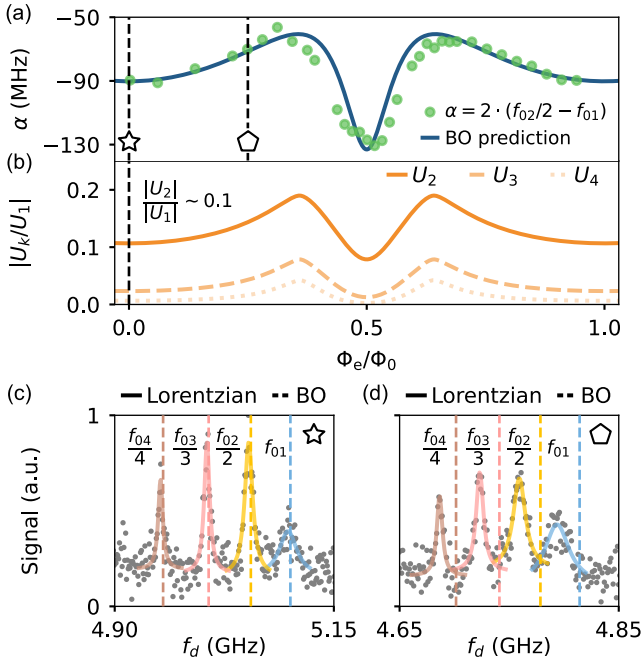


FIG. 3. Measured anharmonicity as a function of flux and extracted harmonic content of the tunable double-junction transmon (second cooldown). (a) Measured anharmonicity (green) compared with the Born–Oppenheimer (BO) prediction (blue). Vertical dashed lines mark  $\Phi_e = 0$  and  $\Phi_e = 0.25\Phi_0$ . (b) Extracted second, third, and fourth harmonics normalized to the first harmonic from the BO model; at  $\Phi_e = 0$  we obtain  $U_k = [1, 0.107, 0.023, 0.006]$ . (c) Four observed transitions at  $\Phi_e = 0$  with Lorentzian fits (solid) and BO-predicted frequencies (dashed), showing good agreement. (d) Four observed transitions at  $\Phi_e = 0.25\Phi_0$ ; here the BO model captures the relative level spacings (anharmonicity) but not the absolute transition frequencies.

model for the qubit mode is given by

$$H_{\text{BO}} = 4E_C^q n_q^2 + U_{\text{red.}}(\phi_q) + U_{\text{BO}}(\phi_q). \quad (10)$$

The harmonic content of this BO model can be extracted via

$$U_k = \frac{1}{\pi} \int_{-\pi}^{\pi} [U_{\text{red.}}(\phi_q) + U_{\text{BO}}(\phi_q)] \cos(k\phi_q) d\phi_q. \quad (11)$$

In Fig. 3, we plot the expected anharmonicities from the BO model (blue solid line) together with the measured anharmonicities of the two-mode tunable transmon and find excellent agreement. The second, third and fourth harmonics as a function of  $\Phi_e$  extracted from the BO model can be seen in Fig. 3b. In Fig. 3c, we show a representative qubit spectroscopy measurement at  $\Phi_e = 0$  with Lorentzians centered at the measured transition frequencies (solid lines) and the expected transition frequencies from the BO model (dashed lines). With the excellent agreement between the measured transitions and those extracted from the BO model using the parameters

from the two-mode model fit, we use Eq. (11) to extract harmonics, which results in  $U_k = [1, 0.107, 0.023, 0.006]$  at  $\Phi_e = 0$ . These values are significantly higher than previously observed in single SIS junctions [3–6]. In this device, at  $\Phi_e = 0$ , the junction asymmetry parameter is  $\lambda = 0.85$  and the extracted values of  $U_k$  thus agree quantitatively with those expected from Fig. 1e.

Despite the BO model correctly predicting the anharmonicity across all flux points, it fails to reproduce the measured transition frequencies at  $\Phi_e = 0.25\Phi_0$ , as shown in Fig. 3d (dashed lines). We attribute this discrepancy to the internal mode and higher qubit excitations, which introduce non-perturbative effects not captured within the BO approximation (see Supplementary Material [33], Fig. 6). In contrast, the two-mode model incorporates these higher-order contributions and therefore accurately reproduces the qubit frequency. The total dispersive shift of the readout resonator provides information on the internal-mode dynamics. Extending the two-mode model from Eq. 5 to include dispersive coupling to the resonator (see Supplementary Material [33]), we simultaneously fit  $f_{\text{res}}$  and  $f_{01}$  (gray lines in Fig. 4a) and thereby extract both the internal-mode frequency (purple) and its coupling to the resonator. For all flux values, the qubit transition remains below the bare resonator frequency at 6.378 GHz (red dashed line), implying that the qubit alone would shift the resonator upward. However, in the tunable double-junction transmon, the total dispersive shift is the sum of the qubit contribution  $\chi_q$  and the internal-mode contribution  $\chi_{\text{int}}$  (arrows in Fig. 4a), with analytical expressions provided in the Supplementary Material [33]. At  $\Phi_e = 0$ ,  $\chi_q$  dominates and the resonator shifts upward (Fig. 4b, left). At  $\Phi_e = 0.44\Phi_0$ , the two contributions cancel, resulting in an unchanged resonator frequency despite continued coupling (middle panel). Near  $\Phi_e = \Phi_0/2$ , the internal mode dominates, yielding a net downward shift (right panel). The flux-tunability of the dispersive shift, and in particular the presence of a flux point where the net dispersive shift vanishes, invites further studies for utilizing this effect for next-generation qubit readout [42–46].

In summary, we have realized and characterized a tunable double-junction transmon composed of a SQUID in series with a single SIS junction, enabling *in situ* flux control of the device’s energy-phase relation. We identified flux regimes in which the circuit behaves as a single effective mode and extracted substantially higher-harmonic content, including a second harmonic larger than previously reported for individual SIS junctions. The internal mode associated with the middle-island charging energy plays two central roles: it renormalizes the qubit spectrum, captured in part through a Born–Oppenheimer correction, and it couples dispersively to the readout resonator. Flux-dependent resonator spectroscopy reveals a balance point where the ground-state dispersive shifts induced by the qubit and internal modes cancel, resulting in a vanishing net resonator shift. These results demonstrate that an all-superconducting SIS–SIS platform can

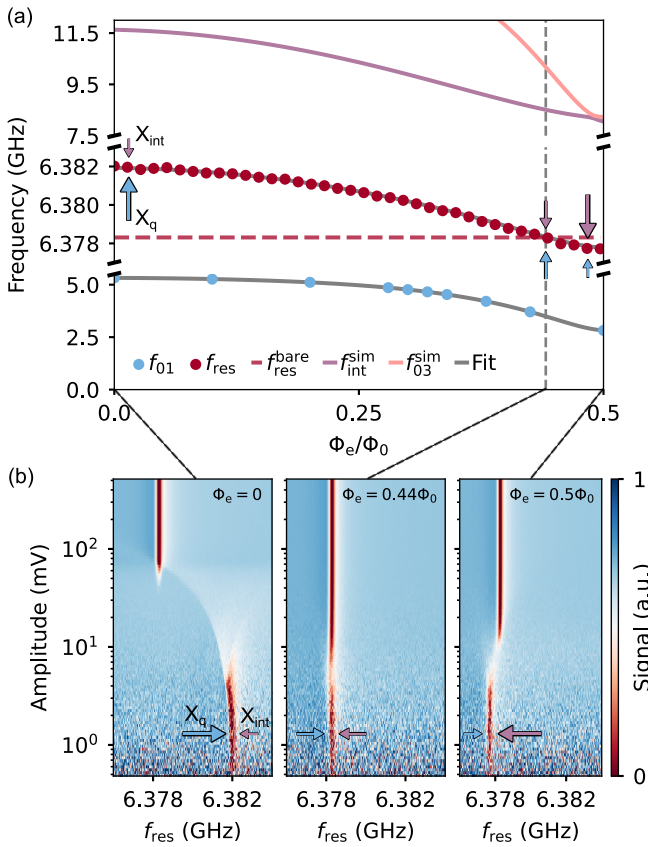


FIG. 4. Flux dependence of the total dispersive shift in the tunable double-junction transmon (first cooldown). (a) Measured data points of the qubit  $f_{01}$  (light blue) and of the resonator  $f_{\text{res}}$  (dark red) with the bare frequency of the resonator  $f_{\text{res}}^{\text{bare}}$  indicated by the red dashed line. Extending the two-mode model from Eq. 5 (see Supplementary Material [33]), we fit  $f_{\text{res}}$  (gray) and extract the simulated internal-mode frequency  $f_{\text{int}}^{\text{sim}}$  (purple) and the qubit's  $f_{03}^{\text{sim}}$  transition, revealing an avoided crossing near  $\Phi_e = \Phi_0/2$ . (b) Resonator spectroscopy versus readout amplitude at three representative flux points. At  $\Phi_e = 0$  (left), the qubit contribution dominates, shifting the resonator upward. At the balance point (middle), the qubit and internal-mode contributions cancel, giving zero net dispersive shift. Near  $\Phi_e = \Phi_0/2$  (right), the internal mode dominates, shifting the resonator downward.

be used to engineer the harmonic content of the Josephson potential, offering a path toward implementing devices such as the  $\cos(2\phi)$  qubit and other protected-qubit designs without the coherence and stability limitations of hybrid superconductor–semiconductor approaches.

## ACKNOWLEDGMENTS

We gratefully acknowledge useful discussions with Valla Fatemi, Christian Andersen, Nataliia Zhurbina and Tyra Cortinez Samenius.

This research was supported by the Novo Nordisk Foundation (grant no. NNF22SA0081175), the NNF Quantum Computing Programme (NQCP), Villum Foundation through a Villum Young Investigator grant (grant no. 37467), the Innovation Fund Denmark (grant no. 2081-00013B, DanQ), the U.S. Army Research Office (grant no. W911NF-22-1-0042, NHyDTech), by the European Union through an ERC Starting Grant, (grant no. 101077479, NovADePro), and by the Carlsberg Foundation (grant no. CF21-0343). Any opinions, findings, conclusions or recommendations expressed in this material are those of the author(s) and do not necessarily reflect the views of Army Research Office or the US Government. Views and opinions expressed are those of the author(s) only and do not necessarily reflect those of the European Union or the European Research Council. Neither the European Union nor the granting authority can be held responsible for them. Finally, we gratefully acknowledge Lena Jacobsen for program management support.

---

[1] A. Blais, A. L. Grimsmo, S. M. Girvin, and A. Wallraff, Circuit quantum electrodynamics, *Rev. Mod. Phys.* **93**, 025005 (2021).

[2] B. Josephson, Possible new effects in superconductive tunnelling, *Physics Letters* **1**, 251 (1962).

[3] D. Willsch, D. Rieger, P. Winkel, M. Willsch, C. Dickel, J. Krause, Y. Ando, R. Lescanne, Z. Leghtas, N. T. Bronn, P. Deb, O. Lanes, Z. K. Minev, B. Dennig, S. Geisert, S. Günzler, S. Ihssen, P. Paluch, T. Reisinger, R. Hanna, J. H. Bae, P. Schüffelgen, D. Grützmacher, L. Buimaga-Iarinca, C. Morari, W. Wernsdorfer, D. P. DiVincenzo, K. Michielsen, G. Catelani, and I. M. Pop, Observation of josephson harmonics in tunnel junctions, *Nature Physics* **20**, 815–821 (2024).

[4] J. Kim, M. Hays, I. T. Rosen, J. An, H. Zhang, A. Goswami, K. Azar, J. M. Gertler, B. M. Niedzielski, M. E. Schwartz, T. P. Orlando, J. A. Grover, K. Seriniak, and W. D. Oliver, Emergent harmonics in josephson tunnel junctions due to series inductance (2025), arXiv:2507.08171 [quant-ph].

[5] Z. Wang, R. W. Parker, E. Champion, and M. S. Blok, High- $e_j/e_c$  transmon qudits with up to 12 levels, *Physical Review Applied* **23**, 10.1103/physrevapplied.23.034046 (2025).

[6] M. Féchant, M. F. Dumas, D. Bénâtre, N. Gosling, P. Lenhard, M. Spiecker, S. Geisert, S. Ihssen, W. Wernsdorfer, B. D’Anjou, A. Blais, and I. M. Pop, Offset charge dependence of measurement-induced transitions in transmons, *Physical Review Letters* **135**, 10.1103/yljv-b4kj (2025).

[7] A. A. Golubov, M. Y. Kupriyanov, and E. Il’ichev, The current-phase relation in josephson junctions, *Rev. Mod. Phys.* **76**, 411 (2004).

[8] T. Larsen, M. Gershenson, L. Casparis, A. Kringshøj, N. Pearson, R. McNeil, F. Kuemmeth, P. Krogstrup, K. Petersson, and C. Marcus, Parity-protected superconductor-semiconductor qubit, *Physical Review Letters* **125**, 10.1103/physrevlett.125.056801 (2020).

[9] A. Gyenis, A. Di Paolo, J. Koch, A. Blais, A. A. Houck, and D. I. Schuster, Moving beyond the transmon: Noise-protected superconducting quantum circuits, *PRX Quantum* **2**, 030101 (2021).

[10] C. Schrade, C. M. Marcus, and A. Gyenis, Protected hybrid superconducting qubit in an array of gate-tunable josephson interferometers, *PRX Quantum* **3**, 030303 (2022).

[11] L. Banszerus, C. Andersson, W. Marshall, T. Linde-mann, M. Manfra, C. Marcus, and S. Vaitiekėnas, Hybrid josephson rhombus: A superconducting element with tailored current-phase relation, *Physical Review X* **15**, 10.1103/physrevx.15.011021 (2025).

[12] R. S. Souto, M. Leijnse, and C. Schrade, Josephson diode effect in supercurrent interferometers, *Phys. Rev. Lett.* **129**, 267702 (2022).

[13] C. Ciaccia, R. Haller, A. C. C. Drachmann, T. Linde-mann, M. J. Manfra, C. Schrade, and C. Schönenberger, Gate-tunable josephson diode in proximitized inas supercurrent interferometers, *Phys. Rev. Res.* **5**, 033131 (2023).

[14] S. Reinhardt, T. Ascherl, A. Costa, J. Berger, S. Gronin, G. C. Gardner, T. Lindemann, M. J. Manfra, J. Fabian, D. Kochan, C. Strunk, and N. Paradiso, Link between supercurrent diode and anomalous josephson effect revealed by gate-controlled interferometry, *Nature Communications* **15**, 10.1038/s41467-024-48741-z (2024).

[15] C. Ishii, Josephson currents through junctions with normal metal barriers, *Progress of Theoretical Physics* **44**, 1525 (1970), <https://academic.oup.com/ptp/article-pdf/44/6/1525/5378760/44-6-1525.pdf>.

[16] Y.-J. Doh, J. A. van Dam, A. L. Roest, E. P. A. M. Bakkers, L. P. Kouwenhoven, and S. De Franceschi, Tunable supercurrent through semiconductor nanowires, *Science* **309**, 272–275 (2005).

[17] M. F. Goffman, C. Urbina, H. Pothier, J. Nygård, C. M. Marcus, and P. Krogstrup, Conduction channels of an inas-al nanowire josephson weak link, *New Journal of Physics* **19**, 092002 (2017).

[18] A. Maiani, K. Flensberg, M. Leijnse, C. Schrade, S. Vaitiekėnas, and R. Seoane Souto, Nonsinusoidal current-phase relations in semiconductor-superconductor-ferromagnetic insulator devices, *Phys. Rev. B* **107**, 245415 (2023).

[19] E. M. Spanton, M. Deng, S. Vaitiekėnas, P. Krogstrup, J. Nygård, C. M. Marcus, and K. A. Moler, Current-phase relations of few-mode inas nanowire josephson junctions, *Nature Physics* **13**, 1177–1181 (2017).

[20] T. W. Larsen, K. D. Petersson, F. Kuemmeth, T. S. Jes-  
persen, P. Krogstrup, J. Nygård, and C. M. Marcus, Semiconductor-nanowire-based superconducting qubit, *Phys. Rev. Lett.* **115**, 127001 (2015).

[21] G. de Lange, B. van Heck, A. Bruno, D. van Woerkom, A. Geresdi, S. Plissard, E. Bakkers, A. Akhmerov, and L. DiCarlo, Realization of microwave quantum circuits using hybrid superconducting-semiconducting nanowire josephson elements, *Physical Review Letters* **115**, 10.1103/physrevlett.115.127002 (2015).

[22] B. Zhang, Z. Li, V. Aguilar, P. Zhang, M. Pendharkar, C. P. Dempsey, J. S. Lee, S. D. Harrington, S. Tan, J. S. Meyer, M. Houzet, C. J. Palmstrøm, and S. M. Frolov, Evidence of  $\phi_0$ -josephson junction from skewed diffraction patterns in sn-insb nanowires, *SciPost Physics* **18**, 10.21468/scipostphys.18.1.013 (2025).

[23] D. Feldstein-Bofill, Z. Sun, C. Wied, S. Singh, B. D. Isakov, S. Krøjer, J. Hastrup, A. Gyenis, and M. Kjaer-gaard, Gatemon qubit revisited for improved reliability and stability, *Phys. Rev. Appl.* **24**, 044099 (2025).

[24] J. M. Chávez-García, F. Solgun, J. B. Hertzberg, O. Jinka, M. Brink, and B. Abdo, Weakly flux-tunable superconducting qubit, *Physical Review Applied* **18**, 10.1103/physrevapplied.18.034057 (2022).

[25] E. Y. Egorova, A. S. Kazmina, and I. N. Moskalenko, A weakly-tunable transmon qubit with an optimized shape of the shunted capacitance, *Pisma v Zhurnal Tekhnicheskoi Fiziki* **50**, 10 (2024).

[26] E. Y. Egorova, A. S. Kazmina, I. A. Simakov, I. N. Moskalenko, N. N. Abramov, D. A. Kalacheva, V. B. Lubsanov, A. N. Bolgar, N. Maleeva, and I. S. Besedin, Three-mode tunable coupler for superconducting two-qubit gates (2025), arXiv:2405.10886 [quant-ph].

[27] J. Hu, A. L. R. Manesco, A. Melo, T. V. Stefanski, C. K. Andersen, and V. Fatemi, Mixed spin-boson coupling for qubit readout with suppressed residual shot-noise dephasing (2025), arXiv:2503.13411 [quant-ph].

[28] P. Sethi, O. Prakash, J.-P. Kaikkonen, M. Kervinen, E. T. Mannila, M. Ribeiro, D. Datta, C. W. Förbom, J. Senior, R. P. Loreto, J. Hätilen, K. Viisanen, J. I. Väyrynen, A. Ronzani, A. Kemppinen, V. Vesterinen, M. Prunnila, and J. Govenius, Native-oxide-passivated trilayer junctions for superconducting qubits (2025), arXiv:2504.03481 [quant-ph].

[29] A. M. Bozkurt, J. Brookman, V. Fatemi, and A. R. Akhmerov, Double-fourier engineering of josephson energy-phase relationships applied to diodes, *SciPost Physics* **15**, 10.21468/scipostphys.15.5.204 (2023).

[30] L. Banszerus, W. Marshall, C. W. Andersson, T. Linde-mann, M. J. Manfra, C. M. Marcus, and S. Vaitiekėnas, Voltage-controlled synthesis of higher harmonics in hybrid josephson junction circuits (2024), arXiv:2402.11603 [cond-mat.mes-hall].

[31] R. C. Jaklevic, J. Lambe, A. H. Silver, and J. E. Mercereau, Quantum interference effects in josephson tunneling, *Phys. Rev. Lett.* **12**, 159 (1964).

[32] P. Krantz, M. Kjaergaard, F. Yan, T. P. Orlando, S. Gustavsson, and W. D. Oliver, A quantum engineer’s guide to superconducting qubits, *Applied Physics Reviews* **6**, 10.1063/1.5089550 (2019).

[33] Supplementary material.

[34] L. Jakobsen, K. Shagalov, D. Feldstein-Bofill, M. Kjaer-gaard, K. Flensberg, and S. Krøjer, (in preparation) (2025).

[35] C. W. J. Beenakker, Universal limit of critical-current

fluctuations in mesoscopic josephson junctions, *Phys. Rev. Lett.* **67**, 3836 (1991).

[36] J. Koch, T. M. Yu, J. Gambetta, A. A. Houck, D. I. Schuster, J. Majer, A. Blais, M. H. Devoret, S. M. Girvin, and R. J. Schoelkopf, Charge-insensitive qubit design derived from the cooper pair box, *Phys. Rev. A* **76**, 042319 (2007).

[37] A. Kringhøj, L. Casparis, M. Hell, T. W. Larsen, F. Kuemmeth, M. Leijnse, K. Flensberg, P. Krogstrup, J. Nygård, K. D. Petersson, and C. M. Marcus, Anharmonicity of a superconducting qubit with a few-mode-josephson junction, *Physical Review B* **97**, 10.1103/physrevb.97.060508 (2018).

[38] V. E. Manucharyan, J. Koch, L. I. Glazman, and M. H. Devoret, Fluxonium: Single cooper-pair circuit free of charge offsets, *Science* **326**, 113 (2009), <https://www.science.org/doi/pdf/10.1126/science.1175552>.

[39] A. Di Paolo, T. E. Baker, A. Foley, D. Sénéchal, and A. Blais, Efficient modeling of superconducting quantum circuits with tensor networks, *npj Quantum Information* **7**, 11 (2021).

[40] A. Ciani, D. P. DiVincenzo, and B. M. Terhal, *Lecture Notes on Quantum Electrical Circuits* (TU Delft OPEN Publishing, 2024).

[41] M. Rymarz and D. P. DiVincenzo, Consistent quantization of nearly singular superconducting circuits, *Phys. Rev. X* **13**, 021017 (2023).

[42] C. Lledó, R. Dassonneville, A. Moulinas, J. Cohen, R. Shillito, A. Bienfait, B. Huard, and A. Blais, Cloaking a qubit in a cavity, *Nature Communications* **14**, 10.1038/s41467-023-42060-5 (2023).

[43] M. H. Muñoz Arias, C. Lledó, and A. Blais, Qubit readout enabled by qubit cloaking, *Phys. Rev. Appl.* **20**, 054013 (2023).

[44] F. Swiadek, R. Shillito, P. Magnard, A. Remm, C. Hellings, N. Lacroix, Q. Ficheux, D. C. Zanuz, G. J. Norris, A. Blais, S. Krinner, and A. Wallraff, Enhancing dispersive readout of superconducting qubits through dynamic control of the dispersive shift: Experiment and theory, *PRX Quantum* **5**, 10.1103/prxquantum.5.040326 (2024).

[45] T. V. Stefanski and C. K. Andersen, Flux-pulse-assisted readout of a fluxonium qubit, *Phys. Rev. Appl.* **22**, 014079 (2024).

[46] T. V. Stefanski, F. Yilmaz, E. Y. Huang, M. F. S. Zwanenburg, S. Singh, S. Wang, L. J. Splithoff, and C. K. Andersen, Improved fluxonium readout through dynamic flux pulsing (2024), arXiv:2411.13437 [quant-ph].

## I. FABRICATION AND MEASUREMENT SETUP

The qubit island was patterned from a 200 nm thick Al film evaporated on a high-resistivity silicon substrate, with a capacitance to ground that corresponds to a charging energy of  $E_C/h \approx 305$  MHz. The JJs were fabricated using the double-angle shadow evaporation technique with controlled *in situ* oxidation at a high pressure of 120 mbar which forms a stack of Al/AlO<sub>x</sub>/Al, as illustrated in the scanning electron microscope (SEM) image in Fig. 1c. Due to the thick oxide layer, the JJ area for

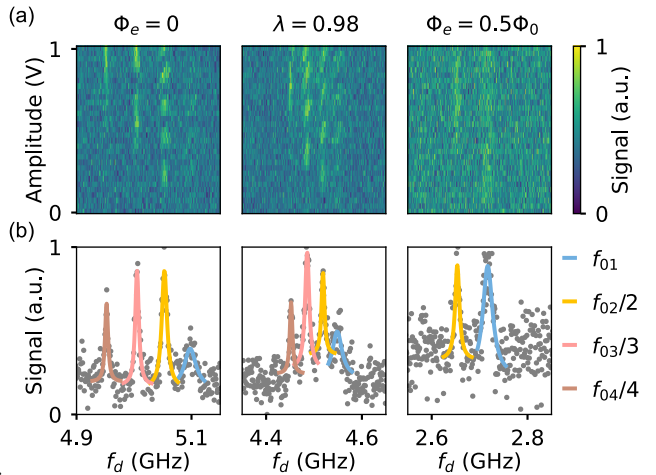


FIG. 5. Extraction of the transitions  $f_{01}$ ,  $f_{02}/2$ ,  $f_{03}/3$  and  $f_{04}/4$  at  $\Phi_e = 0$ , at  $\Phi_e = 0.31\Phi_0$  which corresponds to  $\lambda \approx 0.98$  and at  $\Phi_e = 0.5\Phi_0$  (CD2). (a) Two-tone spectroscopy versus amplitude. (b) Raw data averaged over the amplitude to facilitate the fitting of the transitions to a Lorentzian function.

a given  $E_J$  was designed to be relatively large resulting in a large intrinsic junction capacitance,  $C_{J1}, C_{J2}$ . A patch layer was then deposited to ensure galvanic connection between the SQUID loop, the single JJ, and the rest of the circuit, following the removal of the native aluminum oxide using *in situ* argon milling. Nearby transmission lines facilitate qubit control, with the shorted transmission line regulating the external magnetic flux by adjusting the current, while the open transmission line drives microwave excitations. The qubit is read out using a quarter-wave resonator with a resonance frequency of  $f_{res} = 6.378$  GHz, and a coupling capacitance to the qubit  $C_g = 7.3$  fF. Measurements were performed in a dilution refrigerator with a base temperature of  $\sim 8$  mK.

Measurements were performed over two independent cooldowns of the same device. Data from the first cooldown (CD1) is shown in Figs. 4, 9 and data from the second cooldown (CD2) is shown in Figs. 2, 3, 5, 6, 8. Table I summarizes the parameters that were extracted from the fitting of the spectroscopy measurements as a function of flux to the two-mode model. In the first cooldown (CD1) the parameters were fit to the device coupled to the resonator while fitting  $f_{01}$ ,  $f_{02}/2$  and  $f_{res}$  in parallel. In the second cooldown (CD2) we used the capacitances found in the first cooldown and fit only the Josephson energies which changed compared to CD1 due to the aging of the junctions.

## II. DATA ANALYSIS

Figure 5 presents the data analysis that was done in order to extract the transition frequencies from the raw data. We started from performing a two-tone power spec-

	$C$ (fF)	$E_{J1}$ (hGHz)	$C_{J1}$ (fF)	$E_{JA}$ (hGHz)	$C_{JA}$ (fF)	$E_{JB}$ (hGHz)	$C_{JB}$ (fF)	$f_{res}^{\text{bare}}$ (GHz)	$C_g$ (fF)	$C_r$ (pF)
CD1	63.3	25.7	27.8	31.9	34.5	23.6	25.6	6.3783	7.3	1.2
CD2	63.3	23.4	27.8	30.0	34.5	22.2	25.6			

TABLE I. Device parameters in the first cooldown (CD1) and the second cooldown (CD2) extracted from fitting of the transition frequencies as a function of flux to the two-mode model. 1) Qubit island capacitance. 2) Josephson energy of the single junction. 3) Capacitance of the single junction. 4) Josephson energy of the left junction in the SQUID loop. 5) Capacitance of the left junction in the SQUID loop. 6) Josephson energy of the right junction in the SQUID loop. 7) Capacitance of the right junction in the SQUID loop. 8) Bare resonator frequency. 9) Qubit-resonator coupling capacitance. 10) Resonator self-capacitance.

troscopy at each specific flux point, where in this figure we present the data for the points at  $\Phi_e = 0$ , at a flux which corresponds to  $\lambda \approx 1$ , and at  $\Phi_e = 0.5\Phi_0$ . Next, the signal was averaged over the amplitude to reduce background noise, where the range of amplitudes was adapted according to the transition. Finally, we fit a Lorentzian to each one of the transitions and extracted the frequency. Near  $\Phi_e = 0.5\Phi_0$  we were only able to measure two transitions,  $f_{01}$  and  $f_{02}/2$ .

Figure 6a presents all four transitions ( $f_{01}$ ,  $f_{02}/2$ ,  $f_{03}/3$ ,  $f_{04}/4$ ) that were measured as a function of flux. The lowest two transitions ( $f_{01}$ ,  $f_{02}/2$ ) were fit using the full two-mode model described in Section III, which provided a good prediction for the  $f_{03}$ ,  $f_{04}$  transitions (dotted gray lines). Using the parameters extracted from the fit we simulated the first excited state of the internal mode (purple).

The discrepancy between the extracted transition frequencies from the Lorentzian fitting of the data and the two-mode, BO and reduced models can be seen in Fig. 6b. We observe a good fitting to the full two-mode model across all flux values with the average difference in frequency being  $\sim 6$  MHz and with only two flux points having a difference of above  $\sim 20$  MHz. For the BO model we observe an equally good fit as for the two-mode model next to  $\Phi_e = 0$ , but closer to  $\Phi_e = 0.5\Phi_0$  the model diverges up to  $\sim 200$  MHz compared to the measured values. This effect can be explained by the near avoided-crossings of the internal mode with the second and third excited qubit states near  $\Phi_e \approx 0.31\Phi_0$  and  $\Phi_e \approx 0.47\Phi_0$ , respectively (see Fig. 6a), since the BO model does not capture these non-perturbative interactions. The reduced model diverges at all flux values with a difference of above  $\sim 100$  MHz. Despite the differing levels of agreement with the measured transition frequencies shown in Fig. 6b, the flux dependence of the anharmonicity is nearly identical for all three models, as can be seen in Fig. 6c. This is because the  $f_{01}$  and  $f_{02}/2$  transitions are shifted by approximately the same amount in both the BO and reduced models. The discrepancy between the anharmonicity extracted from the reduced model in Fig. 2b and in Fig. 6c arises from the use of the analytical expression in the former and the numerical model in the latter.

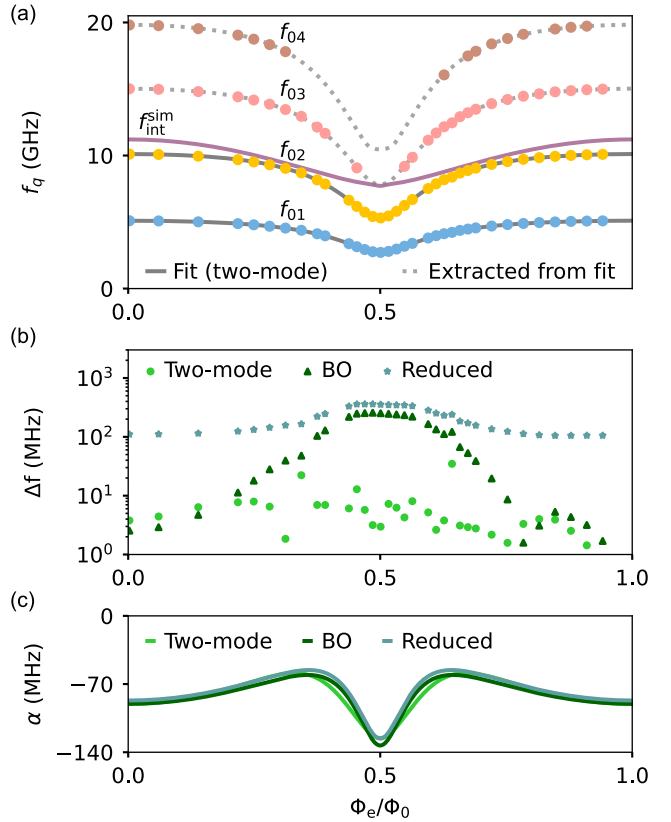


FIG. 6. Measurement of the four transitions as a function of external flux (CD2) with the fit to the two-mode model and the fit error for each of the models. (a) Measurement of the four observed transitions which were extracted from the raw data, with the lowest two transitions being used to fit the data to the full two-mode model from Eq. 5. Simulation of the internal mode first excited state using the parameters extracted from the fit. (b) Fit error of the two-mode, BO and reduced models, compared to the measured values. (c) Anharmonicity as a function of flux using the extracted fit parameters in the two-mode, BO and reduced models.

### III. FULL CIRCUIT ANALYSIS

Here we perform a full circuit analysis of the double-junction transmon coupled to a resonator as illustrated in Fig. 1a. The Lagrangian of our system is of the form,

$$\mathcal{L} = T(\{\dot{\Phi}\}) - U(\{\Phi\}), \quad (12)$$

where  $T$  and  $U$  are the kinetic and potential energies respectively [40]. We work in the  $\Phi_1, \Phi_2, \Phi_r$ -basis, where  $\Phi_1, \Phi_2$  are the flux differences across the single junction and the SQUID respectively, corresponding to the reduced phase variables  $\phi_i = 2\pi\Phi_i/\Phi_0$  for  $i = 1, 2$  defined in Fig. 1a, and  $\Phi_r$  is the flux difference across the quarter-wave resonator which is modelled as a capacitor,  $C_r$ , in parallel with an inductor,  $L$ . The kinetic energy of the device in this basis can be written as,

$$T = \frac{C}{2}(\dot{\Phi}_1 + \dot{\Phi}_2)^2 + \frac{C_{J1}}{2}(\dot{\Phi}_1)^2 + \frac{C_{J2}}{2}(\dot{\Phi}_2)^2 + \frac{C_r}{2}(\dot{\Phi}_r)^2 + \frac{C_g}{2}(\dot{\Phi}_r - \dot{\Phi}_1 - \dot{\Phi}_2)^2, \quad (13)$$

where  $C$  corresponds to the capacitance of the qubit island to ground,  $C_{Ji}$  corresponds to the self-capacitance for the single junction and the SQUID respectively and  $C_g$  to the coupling between qubit and the resonator. The potential energy term is given by,

$$U(\Phi_1, \Phi_2, \Phi_r) = -E_{J1} \cos\left(\frac{2\pi\Phi_1}{\Phi_0}\right) - E_{J2}(\phi_e) \cos\left(\frac{2\pi\Phi_2}{\Phi_0}\right) + \frac{1}{2L}\Phi_r^2, \quad (14)$$

where  $\phi_e = 2\pi\Phi_e/\Phi_0$  with  $\Phi_e$  being the external flux applied through the SQUID loop. We define the corresponding charge term for each of the flux terms:

$$Q_1 = (C + C_{J1} + C_g)\dot{\Phi}_1 + (C + C_g)\dot{\Phi}_2 - C_g\dot{\Phi}_r, \quad (15)$$

$$Q_2 = (C + C_g)\dot{\Phi}_1 + (C + C_{J2} + C_g)\dot{\Phi}_2 - C_g\dot{\Phi}_r, \quad (16)$$

$$Q_r = (C_r + C_g)\dot{\Phi}_r - C_g(\dot{\Phi}_1 + \dot{\Phi}_2). \quad (17)$$

Now, we can write the capacitance matrix of the device as,

$$\mathbb{C} = \begin{pmatrix} C + C_{J1} + C_g & C + C_g & -C_g \\ C + C_g & C + C_{J2} + C_g & -C_g \\ -C_g & -C_g & C_r + C_g \end{pmatrix}.$$

The Hamiltonian of the system can be derived using,

$$H_{\text{full}} = \frac{1}{2}Q^T \mathbb{C}^{-1} Q + U(\Phi_1, \Phi_2, \Phi_r). \quad (18)$$

Introducing the dimensionless charge and phase variables,  $n = Q/(2e)$  and  $\phi = 2\pi\Phi/\Phi_0$ , respectively, we can rewrite the Hamiltonian as,

$$H_{\text{full}} = 4E_{C1}n_1^2 + 4E_{C2}n_2^2 + 4E_C^r n_r^2 + g_{12}n_1n_2 + g_{1,r}n_1n_r + g_{2,r}n_2n_r + U(\phi_1, \phi_2, \phi_r) \quad (19)$$

$$U(\phi_1, \phi_2, \phi_r) = -E_{J1} \cos \phi_1 - E_{J2}(\phi_e) \cos \phi_2 + \frac{E_L}{2}\phi_r^2, \quad (20)$$

with

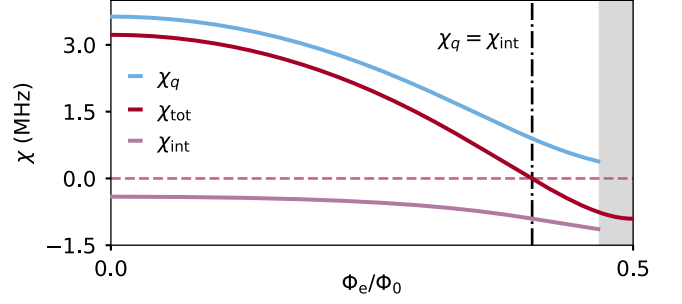


FIG. 7. Simulation of the dispersive shift,  $\chi_0$ , as a combination of the dispersive shift applied by the qubit mode and by the internal mode as a function of flux. The dotted-dashed line represents the flux value where the total dispersive shift is cancelled. The gray area represents the flux values where there is an avoided crossing between the  $f_{01}$  of the internal mode and the  $f_{03}$  of the qubit mode.

where  $E_L = \Phi_0^2/(4\pi^2L)$  is the inductive energy of the resonator.

The charging energies and couplings are defined as follows,

$$E_{Ci} = \frac{e^2}{2} \frac{C + C_{Jj}}{C'(C_1 + C_2) + C_1C_2}, \quad (21)$$

$$E_C^r = \frac{e^2}{2} \frac{C'' + C_g}{C''(C_g + C_r) + C_gC_r}, \quad (22)$$

$$g_{i,r} = 4e^2 \frac{C_{Jj}C_g}{(C_g + C_r)(C'(C_1 + C_2) + C_1C_2)}, \quad (23)$$

$$g_{12} = -4e^2 \frac{C'}{C'(C_1 + C_2) + C_1C_2}, \quad (24)$$

for  $i, j = 1, 2$  and  $i \neq j$ , with  $C' = C + C_gC_r/(C_g + C_r)$  and  $C'' = C + C_{J1}C_{J2}/(C_{J1} + C_{J2})$ .

The full Hamiltonian makes it possible to study the interaction between the resonator and the double-junction transmon. Applying a Schrieffer-Wolff transform [1] allows us to calculate the total dispersive shift  $\chi_0 = \chi_q + \chi_{\text{int}}$  applied by the first excited states of the qubit mode,  $\chi_q$ , and of the internal mode,  $\chi_{\text{int}}$ . Each contribution can be calculated through,

$$\chi_q = \frac{hf_r}{16E_C^r} \frac{|g_{1,r}\mu_{10,1} + g_{2,r}\mu_{10,2}|^2}{\Delta_{10}}, \quad (25)$$

$$\chi_{\text{int}} = \frac{hf_r}{16E_C^r} \frac{|g_{1,r}\mu_{01,1} + g_{2,r}\mu_{01,2}|^2}{\Delta_{01}}, \quad (26)$$

where  $\mu_{ij,k} = \langle i_{qj\text{int}} | n_k | 0_q 0_{\text{int}} \rangle$  for  $i, j = 0, 1$ ,  $k = 1, 2$ ,  $hf_r = \sqrt{8E_C^r E_L}$  and  $\Delta_{ij} = f_r - f_{ij}$ .

Figure 7 shows that the contribution of the qubit mode and the internal mode to the total dispersive shift are

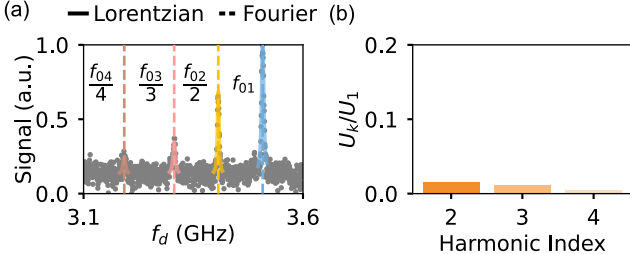


FIG. 8. Two-tone spectroscopy of a traditional single-junction transmon as a reference device, and its extracted harmonic content (CD2). (a) Two-tone spectroscopy showing four qubit transitions with Lorentzians around the measured transition frequency (solid lines) and the extracted frequencies (dashed lines) from the fit to the phenomenological model,  $H_T = 4E_C n^2 - \sum_{k=1}^4 U_k \cos(k\phi)$ . (b) The extracted harmonic content from the fitting to the phenomenological model.

opposite in their sign. We can see that at  $\Phi_e = 0$  the main contribution arises from the qubit mode, then there is a point in flux where they exactly cancel each other out and finally near  $\Phi_e = 0.5\Phi_0$  the main contribution comes from the internal mode, corresponding to what the measurements have shown in Fig. 4. At  $\Phi_e = 0.5\Phi_0$  we were not able to extract the contribution of each of the modes separately due to an avoided crossing between the  $f_{01}$  of the internal mode and the  $f_{03}$  of the qubit mode.

#### IV. BORN-OPPENHEIMER APPROXIMATION

Here we review the Born-Oppenheimer approximation of the double-junction circuit following Ref. [34]. In order to apply the Born-Oppenheimer approximation, we work in the qubit and internal-mode basis [41], with  $\phi_q = \phi_1 + \phi_2$  and  $\phi_{\text{int}} = (C_{J2}\phi_2 - C_{J1}\phi_1)/(C_{J1} + C_{J2})$ . After plugging these definitions into the expression for the kinetic energy of the device we can rewrite the capacitance matrix in the new basis,

$$\mathbb{C}_{\text{q}}^{\text{int}} = \begin{pmatrix} C + \frac{C_{J1}C_{J2}}{C_{J1} + C_{J2}} + C_g & 0 & -C_g \\ 0 & C_{J1} + C_{J2} & 0 \\ -C_g & 0 & C_r + C_g \end{pmatrix}.$$

Now we can also write the Hamiltonian in the new basis where the coupling terms between the internal mode and the resonator and between the two modes disappear.

$$H(\phi_q, \phi_{\text{int}}, \phi_r) = 4E_C^q n_q^2 + 4E_C^{\text{int}} n_{\text{int}}^2 + 4E_C^r n_r^2 + gn_q n_r + U(\phi_q, \phi_{\text{int}}, \phi_r). \quad (27)$$

The charging energies and couplings are now defined as follows,

$$E_C^q = \frac{e^2}{2(C' + C'')}, \quad (28)$$

$$E_C^{\text{int}} = \frac{e^2}{2(C_{J1} + C_{J2})}, \quad (29)$$

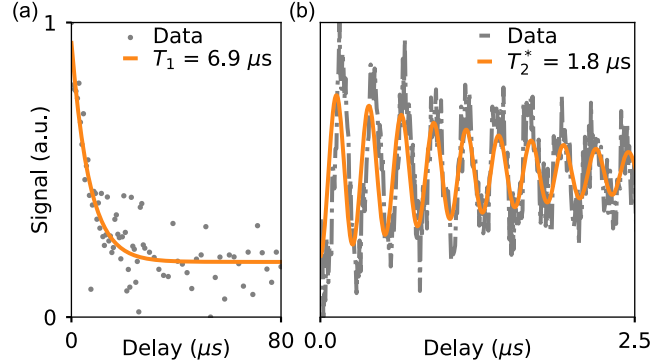


FIG. 9. Coherence data at  $\Phi_e = 0$  (CD1). (a) Qubit relaxation time measurement which was fit to be  $T_1 = 6.9 \mu\text{s}$ . (b) Ramsey interferometry measurement. The qubit dephasing time was fit to be  $T_2^* = 1.8 \mu\text{s}$ .

$$E_C^r = \frac{e^2}{2} \frac{C'' + C_g}{(C' + C'')(C_g + C_r)}, \quad (30)$$

$$g = 4e^2 \frac{C_g}{(C' + C'')(C_g + C_r)}. \quad (31)$$

To obtain the effective one-dimensional Hamiltonian from Eq. 9, we apply a Born-Oppenheimer approximation that exploits the energy separation between the fast internal mode  $\phi_{\text{int}}$  and the slow collective mode  $\phi_q$ . For each value of  $\phi_q$ , the internal coordinate  $\phi_{\text{int}}$  is assumed to remain in its ground state, thereby dressing the Josephson energy experienced by the qubit coordinate. Treating  $\phi_q$  as a classical parameter, we minimize the potential with respect to  $\phi_{\text{int}}$  and expand it around  $\phi_{\text{int}} = 0$ , yielding a harmonic Hamiltonian for the fast mode. The ground-state energy,

$$E_0(\phi_q) \approx -E_{J\Sigma} \sqrt{1 - \lambda \sin^2(\phi_q/2)} - E_{J\Sigma} \sqrt{\frac{2E_C^{\text{int}}}{E_{J\Sigma}}} \sqrt{1 - \lambda \sin^2(\phi_q/2)} \quad (32)$$

acts as an effective potential for  $\phi_q$ , corresponding to Eq. 9. The resulting one-dimensional Hamiltonian is therefore

$$H_{\text{BO}}(\phi_q, \phi_r) = 4E_C^q n_q^2 + 4E_C^{\text{int}} n_{\text{int}}^2 + \frac{E_L}{2} \phi_r^2 + gn_q n_r + E_0(\phi_q). \quad (33)$$

Physically, the Born-Oppenheimer procedure integrates out the high-frequency internal oscillation, renormalizing the Josephson energy and introducing a small correction of order  $(E_C^{\text{int}}/E_{J\Sigma})^{1/2}$  that captures the zero-point motion of the fast mode.

#### V. FIXED-FREQUENCY TRANSMON DATA

To provide a comparison for the expected harmonic content of an SIS junction, we fabricated and measured

a fixed-frequency transmon. We were able to observe four transitions as can be seen in Fig. 8a. To extract the harmonic content of this device we fit the spectra to a phenomenological model,  $H_T = 4E_C n^2 - \sum_{k=1}^4 U_k \cos(k\phi)$ , from which we extracted the transitions which can be seen as dashed lines. The extracted harmonics are presented in Fig. 8b, where we observe very low harmonic content for  $k > 1$ ,  $U_k = [1, 0.015, 0.011, 0.005]$ , corresponding to previously reported values for SIS junctions.

## VI. COHERENCE

Figure 9 shows coherence data which was measured at  $\Phi_e = 0$ . This data is representative of a series of coherence measurements which were done at different flux points and resulted in the qubit relaxation time,  $T_1$ , between 4  $\mu$ s and 13  $\mu$ s. Due to increasing flux noise it was challenging to perform an adequate fitting of the qubit dephasing time away from the flux sweet spots. Fig. 9b shows a characteristic Ramsey interferometry measurement which resulted in  $T_2^* \sim 1.8 \mu$ s.